Check for updates

Quantitative Scanning Transmission Electron Microscopy–High-Angle-Annular Dark-Field Study of the Structure of Pseudo-2D Sb_2Te_3 Films Grown by (Quasi) Van der Waals Epitaxy

Vitomir Sever, Nicolas Bernier, Damien Térébénec, Chiara Sabbione, Jessy Paterson, Florian Castioni, Patrick Quéméré, Audrey Jannaud, Jean-Luc Rouvière, Hervé Roussel, Jean-Yves Raty, Françoise Hippert, and Pierre Noé**

Scanning transmission electron microscopy (STEM) techniques are used to improve the understanding of out-of-plane oriented Sb_2Te_3 thin films deposited by sputtering on SiO_2 and Si substrates. Nanobeam precession electron diffraction, energy-dispersive X-ray spectroscopy, and high-angle-annular dark-field imaging show that the presence of 1–2 atomic planes of Te on top of the substrate is a crucial factor for successful growth of such films, which can be achieved by optimizing cosputtering of Te and Sb_2Te_3 targets. The formation of an actual van der Waals (vdW) gap between the substrate and the first Sb_2Te_3 quintuple layer allows for vdW epitaxy. This gap is larger than those separating Te planes in the pseudo-2D Sb_2Te_3 structure. HAADF image analysis provides detailed information on the atomic arrangement such as interplanar distances, vdW gaps, and Debye–Waller coefficients, all these with a few pm precision. For the anisotropic atomic displacements, a new methodology is introduced based on the statistical analysis of atomic column positions that provides information on the low-frequency phonon modes. Ab initio calculations are used to support our results. Overall, this study provides quantitative STEM tools particularly well suited for nonperiodic pseudo-2D materials, such as Sb_2Te_3/GeTe superlattices.

1. Introduction

The rise of Internet of Things (IoT) devices and technological trends such as artificial intelligence and machine learning is creating a growing demand for improved performance in computing technologies. Thus, fast, nonvolatile memory technologies are needed for both data processing and storage in order to handle the huge amounts of data at lower environmental cost. One of the most promising alternatives for storage class memory, which aims to bridge the technology gap between DRAM and NAND Flash memories, are phase-change memories (PCMs).[1] In a standard PCM, a small volume of a chalcogenide phase-change material (e.g., a $Ge_2Sb_2Te_5$ alloy) rapidly and reversibly changes from an amorphous state (memory RESET state 0) to a polycrystalline state (memory SET state 1). However, one of the main limitations of standard PCMs is the high RESET current required for a melting–quenching process to locally amorphize the phase-change material.[2,3] Thus, reducing power consumption in PCMs is currently the priority of many research groups. The integration of a GeTe/Sb_2Te_3 superlattice (SL) into a memory cell has resulted in a significant reduction in RESET current compared to similar devices incorporating reference phase-change alloys such as $Ge_2Sb_2Te_5$ or GeTe.[4,5]

V. Sever, N. Bernier, D. Térébénec, C. Sabbione, J. Paterson, F. Castioni, P. Quéméré, A. Jannaud, P. Noé
University Grenoble Alpes
CEA
LETI
F-38000 Grenoble, France
E-mail: nicolas.bernier@cea.fr; pierre.noe@cea.fr

J.-L. Rouvière
University Grenoble Alpes
CEA
IRIG
F-38000 Grenoble, France

H. Roussel, F. Hippert
University Grenoble Alpes
CNRS
Grenoble INP
LMGP
F-38000 Grenoble, France

J.-Y. Raty
Condensed Matter Simulation & CESAM, B5
Université de Liège
B4000 Sart-Tilman, Belgium

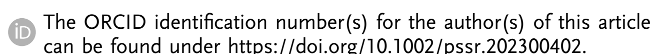
The ORCID identification number(s) for the author(s) of this article can be found under https://doi.org/10.1002/pssr.202300402.

DOI: 10.1002/pssr.202300402

© 2024 Wiley-VCH GmbH

18626270, 0, Downloaded from https://onlinelibrary.wiley.com/doi/10.1002/pssr.202300402 by Thirion Paul - Dge, Wiley Online Library on [20/02/2024]. See the Terms and Conditions (https://onlinelibrary.wiley.com/terms-and-conditions) on Wiley Online Library for rules of use; OA articles are governed by the applicable Creative Commons License

GeTe/Sb_2Te_3 SLs are obtained by alternatively depositing nanometer-thick GeTe and Sb_2Te_3 crystalline layers with atomic planes parallel to the substrate. However, during deposition, Ge atoms diffuse into the Sb_2Te_3 layers to form intermixed blocks (GST) containing Te planes as well as planes with mixed Ge and Sb occupancy. As-deposited SLs consist of a complex, nonperiodic stacking of Sb_2Te_3 blocks (five Te–Sb–Te–Sb–Te atomic planes forming a so-called quintuple layer (QL)) and GST blocks separated by so-called van der Waals (vdW)-like gaps between the Te planes.[6–11] The performance of devices integrating these SLs depends on the precise nature of the stacking of the different blocks. A deeper understanding of the local atomic structure of SLs is therefore mandatory to improve and master this technology.[5]

High-angle-annular dark-field (HAADF)–scanning transmission electron microscopy (STEM) technique has been widely employed in recent years to study the atomic structure of chalcogenide SLs as well as pseudo-2D vdW-layered chalcogenide films such as Sb_2Te_3 or $Ge_2Sb_2Te_5$, for example, to determine defects (swapped bilayers, vacancy layers, twinning domains…),[8,12–14] chemical intermixing,[6–11] or vdW gaps reorganization.[12] The widespread use of this technique for fast, elemental identification is due to its ease of interpretation. Indeed, HAADF images do not suffer from contrast delocalization or contrast inversion. Unlike in high-resolution transmission electron microscopy (TEM), the HAADF experimental intensities allow a clear distinction between elements with very different Z-numbers (e.g., Sb/Te vs. Ge) since the column intensity increases with Z.[15] Most of the studies devoted to SLs are based on a qualitative description of HAADF images that does not require advanced data processing and image simulation tools.[16] Nevertheless, a quantitative analysis can provide much more information, such as atomic column positions with picometer precision,[17] chemical quantification with about 3% precision,[18] or deep insight to the thermal vibrations of the lattice.[19] Therefore, we developed a new Python library in which we combined and implemented well-established methods for measuring atomic column positions and local composition, with precision down to a few picometers. In this work, the tools we developed are applied to the study of Sb_2Te_3 thin films, exploring and discussing innovative insights regarding growth conditions, interplanar distances, vdW gaps, Debye–Waller coefficients, and anisotropic atomic displacements.

2. Python Tools for Quantitative HAADF Imaging

Several tools have been developed by different research groups to determine atomic column positions or local composition from STEM images, such as Atomap,[20] ImageEval,[21] or StatSTEM[22] programs. However, we preferred to develop our own integrated module, not only to extract precise information about both the intensity and position of atomic columns, but also to facilitate the comparison with STEM image simulations and explore original numerical analyses of atomic column positions. The aim of this development is therefore to facilitate, promote, and provide new quantitative studies of the local atomic structure, especially in the case of SLs and pseudo-2D vdW-layered chalcogenide films. For that purpose we developed a new Python library in which we combined and implemented well-established methods for measuring atomic column positions and local composition, as it will be briefly explained in the following sections. A more detailed description is given in Supporting Information S1.

The template matching (TeMA) approach proposed by Zuo et al.[23] is used to measure column positions with subpixel accuracy. Since TeMA can run from templates extracted from each experimental image, this Python tool has been specifically optimized to be robust when applied to nonperiodic and defect-containing structures such as SLs or pseudo-2D vdW-layered chalcogenide films. We show in the following that this approach allows measuring distances between atomic columns with an accuracy down to a few picometers. Here, TeMA is also combined with the quantification approach developed by Rosenauer et al.[24] that consists of comparing the normalized experimental intensities with those simulated (using the frozen-lattice multislice algorithm in the STEMsim program[25] taking into account the nonuniformity of the detector sensitivity) for different TEM foil thicknesses, atomic column compositions, and atomic vibrations. The analysis uses the Voronoï cell method[26] using the precise atomic column positions provided by TeMA. As an evaluation test, the Python code was applied to HAADF–STEM images acquired on a calibration specimen that consists of four 10 nm-thick SiGe layers with Ge concentrations of 45 at%, 38 at%, 31 at%, and 20 at%, each separated by 30 nm of silicon, on a silicon substrate. As shown in Supporting Information S2, the results obtained using our Python code show that the local Ge composition can be measured from STEM images with a relative accuracy of ≈1.6%. Furthermore, since the growth of SiGe layers is epitaxial, this specimen is appropriate for a direct comparison of the measured strain to simulations using finite-element modeling. Indeed, the in-plane lattice spacing does not change while the lattice parameter is distorted along the growth direction as a function of the Ge content. As shown in Supporting Information S2, the STEM-measured strain deviates from the actual strain value by less than 0.2%.

3. Results and Discussion

3.1. Analysis of the Interface between the Substrate and Pseudo-2D Sb2Te3 Thin Films

Our developed tools are applied to the study of Sb_2Te_3 thin films. In addition to being a constituent of chalcogenide SLs and a seed layer for the growth of the SL, Sb_2Te_3 is of great technological interest as it is a topological insulator, which makes it a potential candidate for spinorbitronics applications.[27,28] Besides, Sb_2Te_3 is responsible for the remarkable thermoelectric properties of Sb_2Te_3/Bi_2Te_3 alloys and SLs.[29,30] The growth of out-of-plane oriented Sb_2Te_3 films, thanks to vdW epitaxy, using different deposition techniques, molecular beam epitaxy (MBE), pulsed laser deposition, or sputtering, is well documented in the literature.[31–38] For applications, mastering the growth by industry-compatible methods is essential. Two 400 nm-thick Sb_2Te_3 films were deposited at ≈250 °C by magnetron sputtering in an industrial cluster tool on (100) Si wafers of 300 mm diameter by cosputtering of Sb_2Te_3 and Te targets. As shown in our

© 2024 Wiley-VCH GmbH

18626270, 0, Downloaded from https://onlinelibrary.wiley.com/doi/10.1002/pssr.202300402 by Thirion Paul - Dge, Wiley Online Library on [20/02/2024]. See the Terms and Conditions (https://onlinelibrary.wiley.com/terms-and-conditions) on Wiley Online Library for rules of use; OA articles are governed by the applicable Creative Commons License

previous works,[9,37] the cosputtering method allows to deposit stoichiometric and well out-of-plane oriented Sb_2Te_3 films. One film was deposited after cleaning the surface of the Si substrate by an Ar plasma treatment, which removes the native silicon oxide and leads to the formation of a few nm-thick amorphous Si layer. The other film was deposited on a Si wafer covered with a 100 nm-thick amorphous SiO_2 layer obtained by thermal oxidation of the Si substrate. The SiO_2 surface was cleaned by a soft Ar plasma etching to remove surface contamination before starting the deposition of Sb_2Te_3. X-ray diffraction (XRD) was performed on the two films to check their overall structural quality. The results (given in the Supporting Information S3) show that most of the Sb_2Te_3 crystallites have an out-of plane orientation, with the atomic planes of Sb and Te parallel to the substrate, that is, with the c axis perpendicular to the substrate (hexagonal indexation of the trigonal structure of Sb_2Te_3). No preferential in-plane orientation of the crystallites is present. The lattice parameters a and c are almost identical in both films and close to the values measured on single crystals[39,40] or powdered Sb_2Te_3 samples,[41] as reported in the Supporting Information S4.

We acquired precession electron diffraction (PED) mappings to further examine the microtexture of the films and select a suitable crystallite for quantitative HAADF–STEM studies. This characterization technique, also known as automated crystal orientation mapping (ACOM),[42] allows to measure the orientation of all Sb_2Te_3 grains with a spatial resolution of ≈3 nm. **Figure 1**a, b shows the inverse pole figure (IPF) mappings along the <001> axis of the Si substrate for both Sb_2Te_3 films. The orientation of the silicon substrate is defined within the coordinate system illustrated in Figure 1e. Apart from a very small number of disoriented crystallites, mostly located in the upper part of the films close to their surface, the Sb_2Te_3 grains appear in red in the IPF map, indicating that their c axis is close to the normal to the substrate. In order to acquire high-resolution HAADF–STEM images, the electron beam must be aligned along a crystallographic direction for which the atomic columns and vdW-like gaps of Sb_2Te_3 can be resolved. Here, the <11–20> (hexagonal notation) observation direction is chosen. Therefore, from the orientation data collected in PED mappings, we calculated for each pixel the angular disorientation with respect to this zone axis condition, as schematically illustrated in Figure 1g. Results are shown in Figure 1c,d. In the two films, crystallites with a height equal to the film thickness (≈400 nm) are observed. Their size in the plane of the substrate is of the order of 200 nm. Information on the distribution of the c axis orientation among the crystallites can also be deduced from the analysis of rocking curves measured by XRD on a 00l diffraction peak. The full width at half maxima of the rocking curves are equal to 4.7° and 1.9° for the films deposited on Si and SiO_2, respectively (Supporting Information S3). Although the orientation distribution is larger for the film deposited on Si, this result indicates that well-oriented out-of-plane Sb_2Te_3 films were deposited on both types of substrates. Similar results are observed for Sb_2Te_3 films deposited on amorphous substrates by MBE.[35]

For each film, one crystallite with the smallest possible disorientation with respect to the <11–20> direction was chosen for high-resolution STEM measurements and analysis

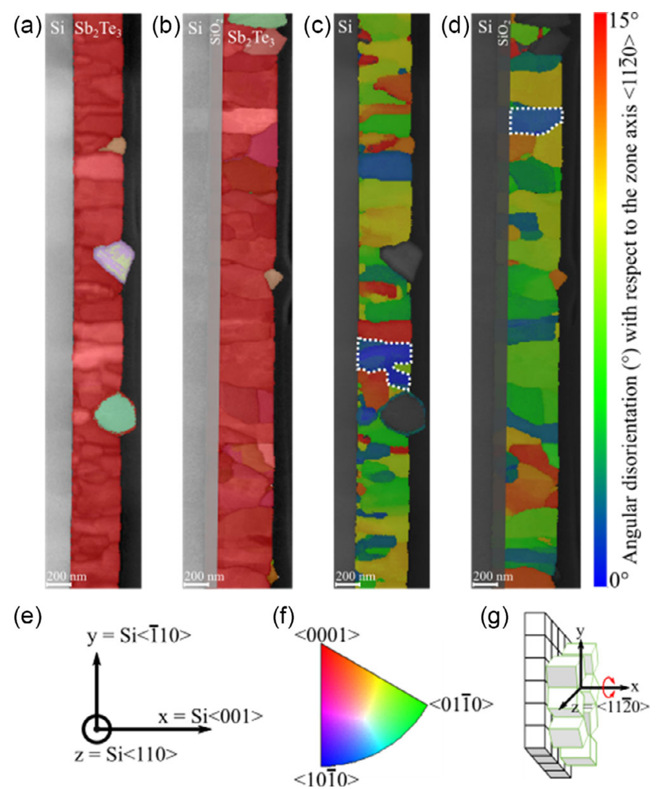

Figure 1. IPF map of the Sb_2Te_3 grains with respect to the silicon <001> axis in films grown on a) deoxidized Si and b) SiO_2 susbtrates. The color legend is given in (f). Angular disorientation map of the Sb_2Te_3 grains with respect to the zone axis <11–20>condition (color bar from blue for 0° disorientation to red for 15° disorientation) in films grown on c) deoxidized Si and d) SiO_2. Sb_2Te_3 grains studied in high-resolution HAADF are evidenced by white dotted lines. e) Coordinate system of the silicon substrate. f) Color legend of the IPF mappings. g) Scheme representing the angular disorientation of the Sb_2Te_3 grains (green) on the substrate (black) with respect to the zone axis <11–20>.

(see Figure 1c,d), and ten high-resolution HAADF images were acquired from the substrate to the top surface. An example of an HAADF image acquired on the Sb_2Te_3 film deposited on amorphous SiO_2 is shown in **Figure 2**a. Only the lower part of the 400 nm-thick film is shown here in order to visualize the interface between the film and the SiO_2 layer. Whereas deposition on crystalline or amorphous Si is well established,[6,7,9,31,33,34,36] deposition on silicon oxide has been more debated. In the case of MBE, the growth of oriented Sb_2Te_3 films could not be achieved on SiO_2 but could be achieved on SiO_x ($x < 2$).[35] In the case of sputtering, deposition on SiO_2 was reported to be impossible[31] but deposition on native silicon oxide was reported.[7] We have shown in ref. [37] that out-of-plane oriented Sb_2Te_3 films can in fact be deposited by sputtering onto various materials, including SiO_2 and SiO_x, when using cosputtering of Te and Sb_2Te_3 targets, which allows the formation of a Te-rich layer on the surface of the bottom material. However, a detailed study of the interface structure between the SiO_2 layer and the first QL of Sb_2Te_3 remains to be done. The presence of an ordered atomic plane on top of the SiO_2 substrate is detected in the HAADF image shown in Figure 2. A well visible gap

 © 2024 Wiley-VCH GmbH

18626270, 0, Downloaded from https://onlinelibrary.wiley.com/doi/10.1002/pssr.202300402 by Thirion Paul - Dge, Wiley Online Library on [20/02/2024]. See the Terms and Conditions (https://onlinelibrary.wiley.com/terms-and-conditions) on Wiley Online Library for rules of use; OA articles are governed by the applicable Creative Commons License

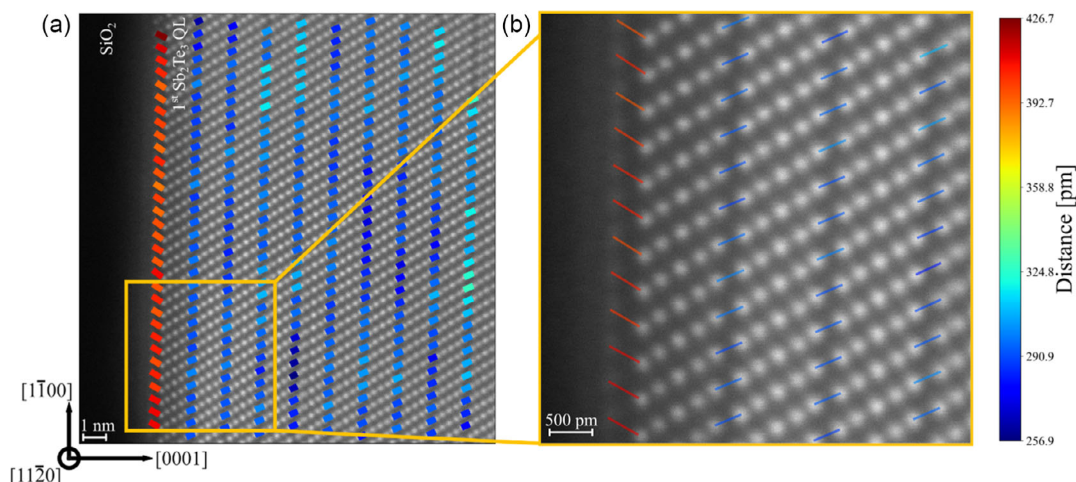

Figure 2. a) HAADF image of a Sb_2Te_3 film grown on SiO_2. b) Enlarged view of the interface between SiO_2 and the first Sb_2Te_3 QLs. The segments represent the measured distance between the two selected Te atomic columns across the vdW gaps. The colors of the segments are chosen according to the color bar shown on the right.

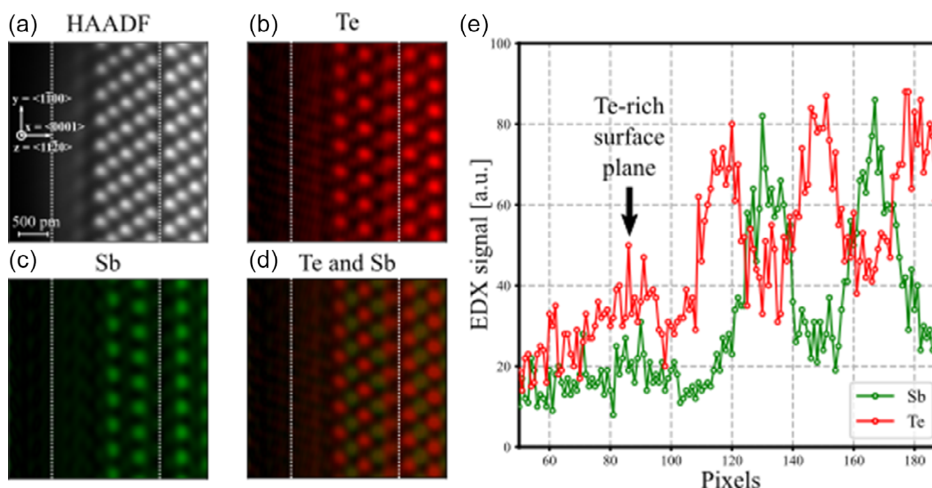

Figure 3. a) HAADF image of the interface between the SiO_2 layer and the Sb_2Te_3 film, showing the presence of a layer comprising atoms with high *Z* numbers. Elemental maps obtained by EDX spectroscopy of b) Te, c) Sb, and d) superimposition of Te and Sb. e) Te and Sb intensity profiles integrated vertically over the whole elemental maps across the passivation layer and the first Sb_2Te_3 QL. On the *x*-axis, 10 pixels correspond to 124 pm.

separates this surface plane from the first QL. One to two surface planes are visible in the EDX mapping of Te but not in that of Sb as shown in **Figure 3**a–d. The chemical concentration profiles of Te and Sb along the growth axis are given in Figure 3e. Since the EDX signal from the surface layer is weak, the EDX spectra are obtained by summing overal pixels in the vertical direction of the image. We observe a slight increase in the overall EDX intensity in the first QL, most likely due to a small disorientation with respect to the electron beam and/or a small thickness gradient of the foil. More importantly, the Te intensity shows a maximum at the pixel positions corresponding to surface planes, while the Sb intensity is constant and equal to the value measured in the SiO_2 layer. A nonzero value of the Sb signal inside the SiO_2 layer can be explained by a contribution due to fluorescence and spurious signals. Thus, within the limit of the experimental accuracy, the atoms in the planes formed on top of the SiO_2 layer are Te atoms and not Sb atoms. Two main reasons may be invoked to account for the low-HAADF intensity of this surface plane: 2) a high level of disorder or defects such as vacancies and 2i) a higher atomic displacement of surface atoms. The fact that the surface plane is mainly composed of Te is reinforced by the analysis of the gap separating this plane from the Te plane of the first Sb_2Te_3 QL. Our developed Python tool, when applied to the HAADF image in Figure 2, provides the shortest distances $d^{\mathrm{Te-Te}}{}_{\mathrm{col}}$ between Te atomic columns across the gaps. All the $d^{\mathrm{Te-Te}}{}_{\mathrm{col}}$ values measured for the gaps between QLs within the image are very close and no variation is detected as a function of the distance between the QL and the substrate. The same conclusion applies when the analysis is extended to all HAADF images acquired throughout the film and the average value of

 © 2024 Wiley-VCH GmbH

$d^{Te-Te}{}_{col}$ is 296.4 ± 1.8 pm. By contrast, the $d^{Te-Te}{}_{col}$-value for the first gap under the first Sb_2Te_3 QL (369.6 ± 7 pm) is significantly larger. A similar trend was observed for Sb_2Te_3 film deposited by MBE on a Si(111)-($\sqrt{3}$x$\sqrt{3}$)R30°-Sb surface in ref. [6] where the larger intercolumn distance under the first QL was ascribed to the presence of Sb adatoms introduced by surface passivation. In addition, there is a twin boundary[43] between the Te-rich surface plane and the first QL. Note that no other twin boundary is observed in the studied crystallite throughout the film thickness. Within the experimental accuracy, the average distance d between columns along the <$1\bar{1}00$> direction is the same in the surface plane and in all planes of the QLs. Its average value is 368.4 ± 0.9 pm. From the knowledge of $d^{Te-Te}{}_{col}$ and d, one can calculate the interatomic distance $d^{Te-Te}{}_{at}$, as explained in the Supporting Information S5. One finds average $d^{Te-Te}{}_{at}$ values of 426.4 ± 6.3 pm for Te atoms across the first gap and 364.8 ± 1.8 pm for Te atoms across adjacent QLs. The latter value is in good agreement with interatomic distances calculated from diffraction studies of the literature on bulk Sb_2Te_3[39–41](see Table S1 in the Supporting Information S4). Therefore, the Te–Te distance across the first gap is larger by a factor 1.17 than the distance between Te atoms belonging to adjacent Sb_2Te_3 QLs. As pointed out in ref. [44], the Te–Te distance across gaps in Sb_2Te_3 is ≈10% smaller than twice the vdW radius of a Te atom, that is, ≈412 pm,[45] showing that the gaps are not pure vdW gaps and that a significant coupling between QLs exists, giving to Sb_2Te_3, as well as to Bi_2Te_3 and Bi_2Se_3, a pseudo-2D character related to the existence of metavalent bonding in these materials. In contrast, we found here that the Te–Te distance across the first gap is close to twice the vdW radius of a Te atom. These remarkable results demonstrate that the growth of an oriented Sb_2Te_3 film is made possible by the formation of a true vdW gap.

3.2. Interatomic Distances

We present an in-depth analysis of interatomic distances through the thickness of the two Sb_2Te_3 films. Three distinct types of interatomic distances, schematically illustrated in **Figure 4**a, are considered: 1) between Sb and the central Te atom in a QL, denoted $d^{Sb-Te(cent)}{}_{at}$, 2) between Sb and the outer Te atom in a QL, denoted $d^{Sb-Te(ext)}{}_{at}$, and 3) between Te atoms across the gaps, denoted $d^{Te-Te}{}_{at}$. These distances correspond to the shortest ones between atoms belonging to successive atomic planes. Supporting Information S4 provides both an example of HAADF image processing to derive maps of intercolumn distances and a table summarizing the interatomic distance obtained from the analysis of the ten HAADF images acquired at different distances from the substrate within one grain for each film. Within the limits of experimental accuracy, no significant variation in the three types of distances is detected within the grain for the two films (see Supporting Information S4), which shows that there is no substantial strain accommodation in the thin films. Furthermore, there is no discernible difference between the interatomic distances in Sb_2Te_3 films grown on Si or SiO_2. We find that the lattice parameters a and c, calculated from HAADF, are in excellent agreement with the values measured by XRD on both films, confirming the accuracy of our approach.

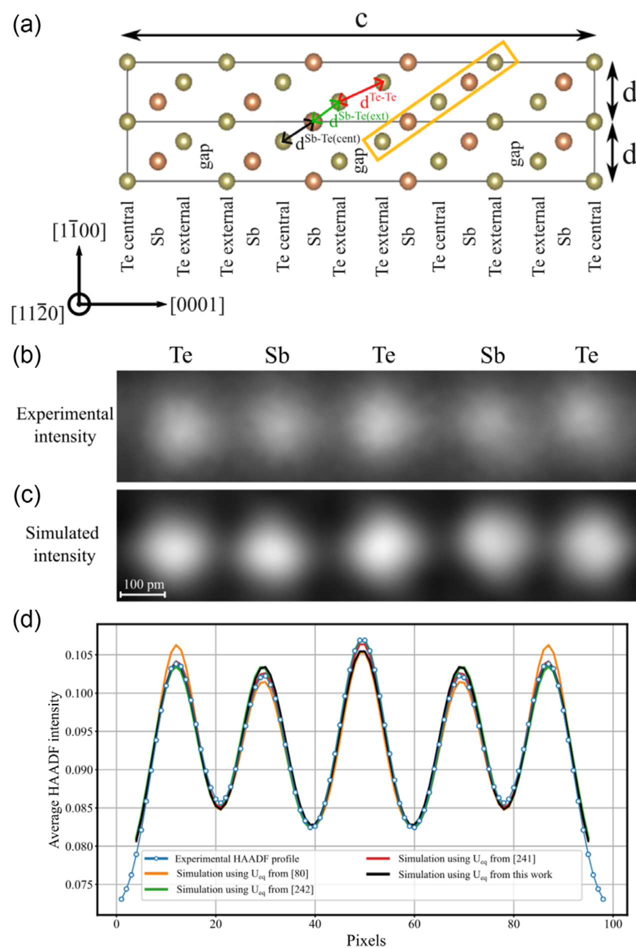

Figure 4. a) Sb2Te3 hexagonal unit cell viewed along the [$11\bar{2}0$] direction. Sb and Te atoms are displayed in orange and green, respectively. Distances $d^{Sb-Te(cent)}$, $d^{Sb-Te(ext)}$, d^{Te-Te} are illustrated schematically with arrows, and the orange rectangular schematic represents a Sb_2Te_3 QL b) Experimental HAADF image of a Sb_2Te_3 QL consisting of Te–Sb–Te–Sb–Te atomic columns, c) Simulated HAADF image of a Sb_2Te_3 QL for a 35 nm-thick foil using U_{eq} from Mansour et al.[41] d) Experimental HAADF intensity profile, averaged over 270 Sb_2Te_3 QLs and simulated profiles using different sets of equivalent isotropic displacement parameters U_{eq}, given in Table 1. [And], [Man], and [Kok] refer to data from Anderson et al.[39] Mansour et al.[41] and Kokh et al.[40] respectively.

The interatomic distances are also in good agreement with values calculated from diffraction studies on bulk Sb_2Te_3[39–41] validating the positions of the atoms in the unit cell deduced from diffraction. Finally, the difference in average length between Sb—Te(ext) and Sb—Te(cent) bonds ($d^{Sb-Te(ext)}{}_{at}$ = 299.6 ± 1.1 versus $d^{Sb-Te(cent)}{}_{at}$ = 315.3 ± 0.4 pm, respectively, for the film deposited on SiO_2) is a consequence of the Peierls distortion in Sb_2Te_3.[44]

3.3. Debye–Waller Coefficients

HAADF images are processed to extract information about the intensity of atomic columns. By averaging the intensity profiles

 © 2024 Wiley-VCH GmbH

18626270, 0, Downloaded from https://onlinelibrary.wiley.com/doi/10.1002/pssr.202300402 by Thirion Paul - Dge, Wiley Online Library on [20/02/2024]. See the Terms and Conditions (https://onlinelibrary.wiley.com/terms-and-conditions) on Wiley Online Library for rules of use; OA articles are governed by the applicable Creative Commons License

of 270 Sb_2Te_3 QLs, an average experimental HAADF intensity profile can be obtained. Note that the Sb_2Te_3 QLs must be precisely oriented along the zone axis in the TEM to obtain symmetric profiles. Yet, very few asymmetric profiles are observed in each image. They are automatically rejected by the program. The average profile for the film grown on SiO_2 shown in Figure 4d reveals that the HAADF intensities of Sb and Te atomic columns are different and, more importantly, that the central Te atomic column has a slightly higher intensity than the Te atomic column near the gaps, as already observed qualitatively in refs. [7,9,46]. In order to interpret these features, simulated HAADF maps are produced using the STEMSim software. To a first approximation, the HAADF intensity depends on three parameters: the thickness of the foil (or the number of atoms per column), the atomic column composition, and the amplitude of the thermal vibrations for each type of atom. Here, we can reasonably assume pure Sb or Te atomic columns, as suggested by the EDX mapping in Figure 3. The thickness of the STEM foil was measured on the Si substrate by position average convergent electron beam diffraction (PACBED)[47] patterns. We found a foil thickness of 35 nm ± 2 nm. In electron microscopy simulation, a key concept is that electron scattering occurs much faster ($\approx 10^{-15}$ s) than the thermal vibrational period of the atoms ($\approx 10^{-13}$ s). Because the time between two successive incoming electrons is long compared to the period of thermal phonon oscillation, the model considers the electron beam to move through a time-averaged electrostatic potential that is the convolution of the electrostatic potential with a Gaussian filter representing the displacement of the atoms.[48] In the case of isotropic atomic displacements, this filter in Fourier space is $f(q) = e^{-2\pi^2 u_{\mathrm{rms}}^2 q^2}$, with q the reciprocal spatial distance and u_{rms} the root mean square displacement of the atoms. We performed simulations using different sets of values for atomic displacements obtained from diffraction studies in the literature[39–41] and given in **Table 1**. Mansour et al.[41] studied the anisotropy of atomic displacements in Sb_2Te_3 by neutron powder diffraction. The STEMsim simulation software only considers isotropically vibrating atoms. Thus, for the simulation, we used the equivalent isotropic displacement parameter U_{eq}, defined as the average of the mean square displacements in the principal directions of the anisotropic displacement ellipsoid.[49] Basically, U_{eq} represents the mean square displacement averaged over all directions. Values of U_{eq} are given in the work of Kohk et al.[40] In the study by Anderson et al.[39] only the mean square displacement in the [0001] direction U_{33} is given. These values were nevertheless used in a STEMsim simulation because, according to Mansour et al. U_{33} and U_{eq} of the three kinds of atoms show similar relative trends.

Simulated HAADF maps, as shown in Figure 4b for a 35 nm-thick lamella, are produced for Sb_2Te_3 samples from 1 to 80 nm thick in 0.425 nm increments. Then, a least-squares minimization of the experimental HAADF profile is performed using all simulated profiles with two free parameters: the width of the Gaussian function used to convolve simulated maps to account for the experimental spatial resolution (Γ_{probe}) and the local foil thickness (t_{foil}), that is not fixed to the measured one in order to test the accuracy of our approach (with respect to the PACBED measurement). Figure 4d shows an excellent agreement between experimental and simulated profiles with U_{eq} values from refs.[40,41] for which the displacement of the central Te atoms is smaller than that of the the external Te atom. As shown in Table 1, we found that the best fit for these two datasets is obtained for t_{foil} values differing by less than 2 nm from the thickness measured by PACBED on Si. In contrast, the profile simulated from Anderson et al.[39] values, for which the displacement of the central Te atom is larger than that of the the external Te atom, differs significantly from the experimental one with a considerably larger square sum of deviations Σ_{dev} as provided in Table 1. This analysis demonstrates that the measured HAADF intensities can only be accurately reproduced if the correct trends of atomic thermal vibrations in the Sb_2Te_3 structure are considered. Note, however, that the profiles simulated using Mansour et al.[41] and Kokh et al.[40] data are quite similar even though the U_{eq} values for the outer Te atoms are quite different, that is, 190 versus 139.6 pm^2, respectively. This result shows a general limitation of the STEM–HAADF quantitative analysis: even by performing this technique to the best of our abilities, it turns out that this is not sufficient to obtain thermal displacements. However, this is not necessarily a negative result. It implies for instance that quantification of Sb and Ge intermixing in $GeTe/Sb_2Te_3$ SLs does not necessarily require to know the exact values of atomic displacements of Sb, Te, and Ge, but only the relative importance of each.

Table 1. Parameters used for fitting the HAADF intensity profile shown in Figure 4. (left) U_{eq} values deduced from X-ray or neutron diffraction studies in the literature (except for Anderson et al.[39] where U_{33} is given). (right) TEM foil thickness (t_{foil}) and probe width (Γ_{probe}) providing the best agreement with the experimental profile for a given set of U_{eq} values. Σ_{dev} is the square sum of the deviations between experimental and simulated profiles. The thickness of the foil measured by PACBED on the silicon substrate is 35 ± 2 nm.

Source	U_{eq} [pm^2]			Quality and parameters of the adjustments		
	Te(cent)	Sb	Te(ext)	t_{foil} [nm]	Γ_{probe} [pm]	Σ_{dev} [a.u.]
From Anderson et al.[39]	101.3	177.3	63.3	30.2	75	0.238
From Mansour et al.[41]	110.0	190.0	190.0	35.3	70	0.175
From Kokh et al.[40]	120.8	184.3	139.6	35.3	72.5	0.132

3.4. Anisotropic Atomic Displacements

The above analysis demonstrates that considering isotropic atomic displacements are sufficient to reproduce experimental HAADF column intensities. We show below that a statistical analysis of atomic column positions gives interesting pieces of information on the anisotropic displacements of atoms. Our methodology, that has been implemented in our python code, shares some common points with previous publications on high-resolution scanning transmission electron microscopy analysis[17,23,50] but our interpretation and results are quite new. **Figure 5** outlines the main steps of our procedure that is an extension of TeMA.[23] When applying TeMA, the positions of each atomic column are determined, and then the six

© 2024 Wiley-VCH GmbH

18626270, 0, Downloaded from https://onlinelibrary.wiley.com/doi/10.1002/pssr.202300402 by Thirion Paul - Dge, Wiley Online Library on [20/02/2024]. See the Terms and Conditions (https://onlinelibrary.wiley.com/terms-and-conditions) on Wiley Online Library for rules of use; OA articles are governed by the applicable Creative Commons License

components of a reference lattice, that is, x and y components of two basis vectors and the origin of the lattice, are calculated by least-squares fitting. Here, the difference with standard TeMA is that a reference lattice is defined for each of the three different types of atoms of the QL: Sb as well as central and external Te. Then, a displacement map is generated for each atom type, as shown in Figure 5d. The 2D displacements are decomposed into directions parallel ($d_{//}$) and perpendicular ($d\perp$) to the gaps, as illustrated in Figure 5a. For the three atom types, the histograms of $d_{//}$ and $d\perp$ are calculated to derive the associated standard deviations $\sigma_{\parallel}^{\text{HAADF}}$ and $\sigma_{\perp}^{\text{HAADF}}$, as shown in Figure 5b. In[JMZ], these standard deviations are used to evaluate the accuracy of the detection of atomic column positions. The originality of our work is to show that these standard deviations can provide information on the anisotropy of atomic displacements. Prior to the presentation of the experimental results, we offer in the subsequent section a theoretical explanation of the observed displacements using our statistical analysis.

The collective atomic vibrations or movements are generally decomposed into orthogonal phonon modes. In practice, these vibrations are studied by spectroscopy techniques and the highest frequency corresponds to the shorted phonon wavelength which is twice the lattice parameter in a cubic structure. In silicon, these high vibration frequencies are in the 10^{12}–10^{13} Hz range which are much faster than our recording times. But, similarly to a lake surface, where H and O atoms vibrate at THz frequencies while at the same time one can observe low-frequencies fluctuation of the water surface, the atoms in the TEM lamella undertake complex collective movements that include phonon modes of many different frequencies ranging from the THz to the few Hz. Physicists generally considered that the low-frequency mode are mainly related to external excitation such as sounds or heat. Importantly, the low-frequency modes follow the same potential and collective constraints as the high-frequency modes and consequently are sensible to the same anisotropy potential constraints. The force magnitude acting on an atomic column in a particular direction is contingent upon the displacements of the surrounding atomic columns, influenced by bond energy and stiffness. In summary, 1) high-resolution HAADF images contain white dots that are correlated

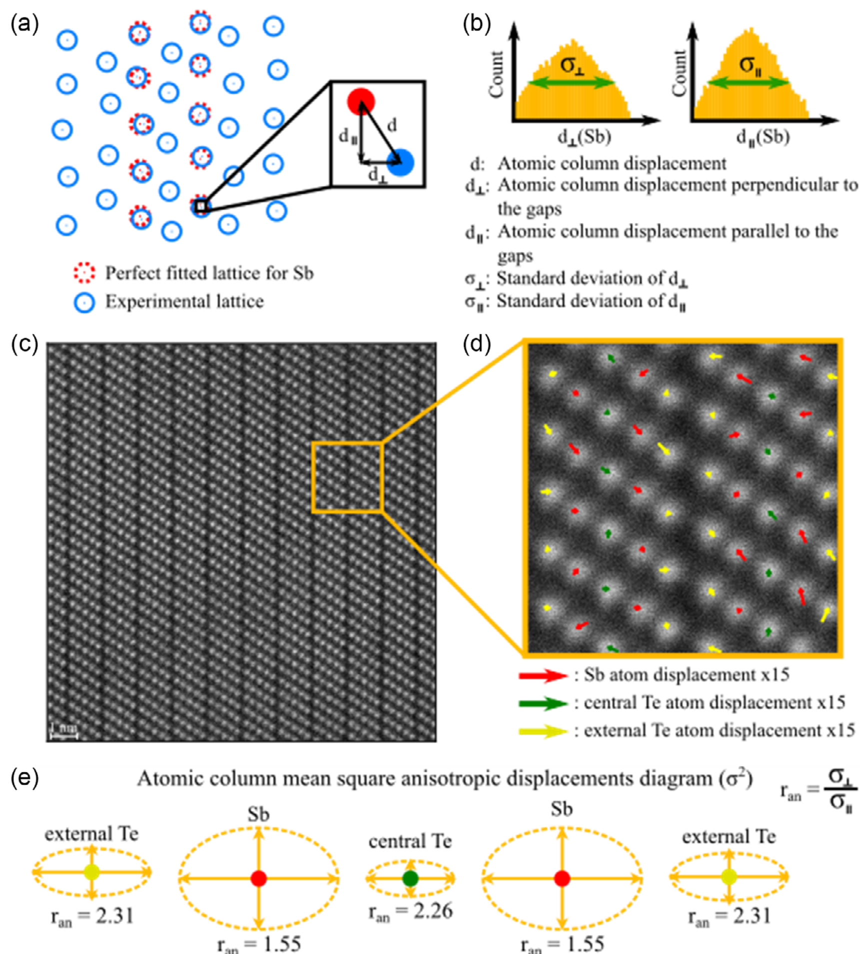

Figure 5. a,b) Principle of the method used to derive mean square displacements of atomic columnss. See text for more details. c,d) Application of the method to an experimental HAADF image acquired on the Sb_2Te_3 film deposited on SiO_2. For better visualization, the length of the arrows is multiplied by a factor of 15. The arrows go from the perfect coordinates to those observed. e) Diagram showing the measured mean square anisotropic displacements of the atoms in the directions parallel and perpendicular to the gaps. The anisotropy factor, equal to $\sigma_{\perp}^2/\sigma_{\parallel}^2$, is referred to as r_{an}.

© 2024 Wiley-VCH GmbH

18626270, 0, Downloaded from https://onlinelibrary.wiley.com/doi/10.1002/pssr.202300402 by Thirion Paul - Dge, Wiley Online Library on [20/02/2024]. See the Terms and Conditions (https://onlinelibrary.wiley.com/terms-and-conditions) on Wiley Online Library for rules of use; OA articles are governed by the applicable Creative Commons License

to the projected average positions of high-frequency vibrating atoms broadened by the experimental tool,[51] 2) these dots have low-frequency oscillations that can be studied either by analyzing a series of image (case 1) or by performing statistical analysis of equivalent dots present in a given STEM image (case 2). In practice, as these low-frequency phonon modes have wavelengths greater than hundred of meters (i.e., larger than the sample size), they can only be activated through external excitations such as external heating or in our case by the incoming electron beam. Electron beam-induced motions have been extensively investigated and documented in recent literature, particularly concerning individual atoms, for example.[52] A quantitative study of the mechanisms involved in atomic column displacements under the electron beam in the TEM is beyond the scope of this article. In what follows, we show that precise statistical measurements of HAADF atomic column positions can provide valuable information on the anisotropic displacements occurring in the material and only case 2, that is, statistics on equivalent dot positions, is realized.

Quantification of $\sigma_{\parallel}^{\mathrm{HAADF}^2}$ and $\sigma_{\perp}^{\mathrm{HAADF}^2}$ from the experimental data is detailed in the Supporting Information S7. We emphasize that atomic displacements were determined using a series of images obtained by varying electron probe currents to address inherent STEM acquisition noise. We also verified that changing the beam scanning direction does not impact the relative atomic displacements. Nevertheless, a comprehensive analysis of all microscope settings, such as high voltage, foil thickness, dwell time, is necessary to accurately determine atomic displacements. In this context, we focus solely on interpreting the relative values of atomic displacement between different atom types. The results are summarized in **Table 2** and **Figure 6**, with a schematic illustration of anisotropy ratios provided in Figure 5e. Note in Table 2 that the measured equivalent isotropic atomic displacement, $\sigma_{\mathrm{eq}}^{\mathrm{HAADF}^2} = \frac{1}{3}(2\sigma_{\parallel}^{\mathrm{HAADF}^2} + \sigma_{\perp}^{\mathrm{HAADF}^2})$, is about 10 times smaller than the experimental value indicating that the low-frequency terms are indeed a small contribution to the total vibrations.

Table 2. Mean square anisotropic displacements of atoms parallel ($U_{\parallel}$) and perpendicular ($U_{\perp}$) to the vdW gaps taken from Mansour et al.[41] and calculated by AIMD simulations in the present work. Equivalent isotropic U_{eq} values are also given. $(\sigma_{\parallel}^{\mathrm{HAADF}})^2$ and $(\sigma_{\perp}^{\mathrm{HAADF}})^2$ are extracted from STEM–HAADF images (see text). $\sigma_{\mathrm{eq}}^{\mathrm{HAADF}^2} = \frac{1}{3}(2\sigma_{\parallel}^{\mathrm{HAADF}^2} + \sigma_{\perp}^{\mathrm{HAADF}^2})$ is an equivalent isotropic atomic displacement.

Source	Properties	Te(cent)	Sb	Te(ext)
From Mansour et al.[41]	$U_{\parallel}$ (pm^2)	120.0	150.0	190.0
	$U_{\perp}$ (pm^2)	70.0	320.0	210.0
AIMD: Without excitation	$U_{\parallel}$ (pm^2)	129	142	156.5
	$U_{\perp}$ (pm^2)	141	249	170
	U_{eq} (pm^2)	133	177.7	161
AIMD: With 0.5 eV excitation	$U_{\parallel}$ (pm^2)	156	167.5	203
	$U_{\perp}$ (pm^2)	159	286	216
	U_{eq} (pm^2)	157	207	207.3
STEM HAADF	$(\sigma_{\parallel}^{\mathrm{HAADF}})^2$ (pm^2)	5	13.1	6.5
	$(\sigma_{\perp}^{\mathrm{HAADF}})^2$ (pm^2)	11.3	20.3	15
	$(\sigma_{\mathrm{eq}}^{\mathrm{HAADF}})^2$ (pm^2)	7.1	15.5	9.3

Importantly, as shown in Figure 6, $\sigma^{\mathrm{HAADF}^2}$ exhibit the exact same trends as U values from,[40] that is, the atomic displacements are highest for Sb atoms and lowest for the central Te atoms. U_{eq} values from ref. [40] provide the best match with experimental HAADF intensities (as shown in Figure 4), so the alignment with this data strengthens the reliability of our statistical positional analysis. In addition, 1) Sb atoms have the largest values of both $\sigma_{\perp}^{\mathrm{HAADF}^2}$ and $\sigma_{\parallel}^{\mathrm{HAADF}^2}$ and 2) $\sigma_{\perp}^{\mathrm{HAADF}^2}$ is larger than $\sigma_{\parallel}^{\mathrm{HAADF}^2}$ for all types of atoms. As shown in Table 2, these findings do not align with those of Mansour et al.[ANM] who reported higher displacement of central Te atoms parallel to the gap compared to the perpendicular direction. Hence, to better understand the HAADF data, we modeled crystalline Sb_2Te_3 using ab initio molecular dynamics (AIMD).

For this purpose, we used the Vienna Ab-initio Simulation Package code,[53] based on density functional theory electronic structure calculations, together with projector augmented wave potentials[54] and the PBESoL exchange-correlation functional.[55] The latter has been found to improve the description of structural and dynamical properties of the related $Ge_1Sb_2Te_4$ and $Ge_2Sb_2Te_5$ compounds, without any inclusion of a semiempirical vdW correction.[56] Indeed, the relaxed hexagonal unit cell parameters (in Å: 4.25; 4.25; 30.18) are close to the experimental values (see Table S1 in the Supporting Information S4). The atoms special positions are (0;0;0.399) for Sb, (0,0,0) for central Te and (0;0;789) for external Te against (0;0;0.3986), (0;0;0) and (0;0;7878) from diffraction.[40,41] The equilibrium interatomic distances are $d^{\mathrm{Sb-Te(ext)}}{}_{\mathrm{at}} = 299$ pm, $d^{\mathrm{Sb-Te(cent)}}{}_{\mathrm{at}} = 315$ pm, and $d^{\mathrm{Te-T)}}{}_{\mathrm{at}} = 363$ pm between external Te atoms across the pseudo-vdW gap. The dynamics was performed at 300 K, on a 240 atom crystal supercell, with Gamma point sampling of the Brillouin zone. A timestep of 3 fs was used together with a Nosé thermostat. Data were acquired and averaged for all specific atomic positions (Sb, Te(cent),Te(ext)) after a 5 ps thermal equilibration and over 10 ps trajectories. In order to probe the possible impact of the incoming electron beam in the TEM, a second AIMD simulation was performed by applying an electronic excitation using constrained density-functional theory, forcing the half occupation of states that initially span a 0.5 eV range around the Fermi level (and preserving the total neutrality).

The simulations provide the components of the mean square displacement tensor from which the projections onto the directions perpendicular and parallel to the gaps defined in the experiment can be calculated. The obtained U_{eq} and anisotropic $U_{\parallel}$, $U_{\perp}$ parameters are given in Table 2 for the two simulations. First, note that trends of AIMD U_{ed} values are in excellent agreement with those from ref. [41] (given in Table1), that is, $U_{\mathrm{Sb}} > U_{\mathrm{Te(ext)}} > U_{\mathrm{Te(cent)}}$. This result confirms the consistency of the AIMD data. In Figure 6, we present the comparison between AIMD U parameters for the two simulations and $\sigma^{\mathrm{HAADF}^2}$. We observe the same trends, in particular, 1) in terms of vibration amplitude, we have $U_{\mathrm{Sb}} > U_{\mathrm{Te(ext)}} > U_{\mathrm{Te(cent)}}$ for both directions (i.e., parallel and normal to the gaps), 2) $U_{\perp}$ parameter is higher than $U_{\parallel}$ for all atom types. Anisotropic vibrations reinforce the idea that the Sb_2Te_3 is indeed a pseudo-vdW material

 © 2024 Wiley-VCH GmbH

18626270, 0, Downloaded from https://onlinelibrary.wiley.com/doi/10.1002/pssr.202300402 by Thirion Paul - Dge, Wiley Online Library on [20/02/2024]. See the Terms and Conditions (https://onlinelibrary.wiley.com/terms-and-conditions) on Wiley Online Library for rules of use; OA articles are governed by the applicable Creative Commons License

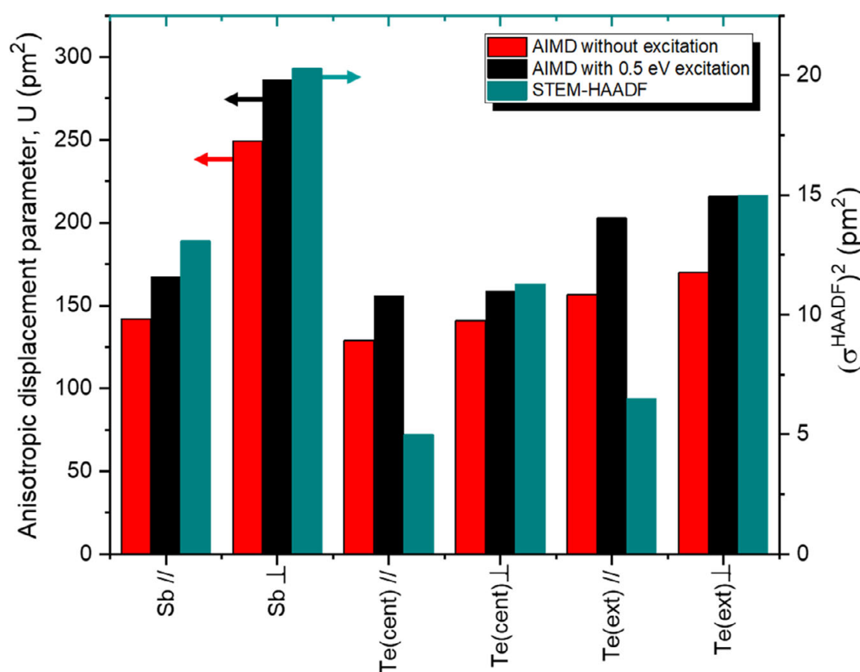

Figure 6. Bar chart showing the AIMD-simulated mean square anisotropic displacements of atoms parallel (//) and perpendicular (⊥) to the vdW gaps (with and without electronic excitation) compared to the mean square column displacements $(\sigma^{HAADF})^2$ measured by HAADF.

for which interplane interactions are weaker than in-plane ones. The 0.5 eV electronic excitation in AIMD systematically leads to a minor increase of all U values, which is especially low for central Te atoms in which case the vibrations under electronic excitation tend to get isotropic probably related to a perfect metavalence (one electron per bond). Overall, we note an excellent qualitative correlation between AIMD U and σ^{HAADF^2} values. Note however that there is a significant difference in the volume electronically excited between TEM experiments (scanning of a sub-Angström electron probe) and AIMD simulations (all the atoms in the supercell). In TEM, the excited atomic column is therefore constrained by ground-state atoms which may limit to a higher extent the atomic displacements. This aspect should also be kept in mind for further analyses.

4. Conclusion

In summary, well-oriented out-of-plane Sb_2Te_3 films were deposited on amorphous SiO_2 and deoxidized Si substrates. By analyzing the interface with the SiO_2 substrate, we have shown that the growth of an oriented Sb_2Te_3 film is made possible by the formation of a true vdW gap between the substrate and the first Sb_2Te_3 QL. Thus, the key parameter for successful growth of an out-of-plane oriented Sb_2Te_3 film on any substrate is the presence of one to two atomic planes consisting mainly or entirely of Te atoms on top of the substrate. This can be spontaneously achieved if the Te flux is sufficient. The present results show that this condition is satisfied when optimized cosputtering of Te and Sb_2Te_3 targets is performed. In this case, the use of a "two-step" method[32,38] where an amorphous Sb_2Te_3 thin seed layer (≈3 nm thick) is first deposited at room temperature and then crystallized by heating is not necessary. Note that successful growth of Sb_2Te_3 on SiO_2 was also found possible by combining the "two-step" method and the use of a single target enriched in Te[38] but no analysis of the interface was performed in that work. The presence of a true vdW gap between the substrate and the first Sb_2Te_3 QL allows the deposition of the first QL by vdW epitaxy. Within the experimental accuracy of the analysis of HAADF images, the structure of the first QL does not differ from that of all other QLs. The quantitative analysis of interatomic distances from HAADF images through the layer thickness showed no measurable strain accommodation in the thin films. The difference of interatomic distances between Sb and Te(ext) or Te(cent) evidences the Peierls distortion in Sb_2Te_3. The presently developed tools for HAADF image analysis allow to determine distances between atomic columns and thus interatomic distances with an accuracy down to a few pm. In the case of a periodic crystal such as Sb_2Te_3, the accuracy on interatomic distances obtained from HAADF image analysis is lower than that obtained from diffraction studies but in the case of nonperiodic structures such as SLs (e.g., comprising various types of GST blocks), our approach will be extremely useful to provide information on the local atomic structure. In addition, we reproduced with good precision the absolute HAADF intensity profile across the Te–Sb–Te–Sb–Te QL. Our analysis unambiguously confirmed that the central Te atoms vibrate less than the outer Te ones. There is however a limitation in the quantitative analysis of HAADF intensities, as it is not possible to extract exact values of isotropic atomic displacements. The HAADF image simulation is sensitive to the relative magnitudes of atomic displacements for each type of atom. This is not necessarily a

© 2024 Wiley-VCH GmbH

18626270, 0, Downloaded from https://onlinelibrary.wiley.com/doi/10.1002/pssr.202300402 by Thirion Paul - Dge, Wiley Online Library on [20/02/2024]. See the Terms and Conditions (https://onlinelibrary.wiley.com/terms-and-conditions) on Wiley Online Library for rules of use; OA articles are governed by the applicable Creative Commons License

negative result. It implies that quantification of Sb and Ge intermixing in GeTe/Sb_2Te_3 SLs does not necessarily require the absolute values of the thermal vibrations of Sb, Te, and Ge, but only the relative importance of each. Finally, anisotropic atomic vibrations were detected using a new methodology that analyzes the statistical positions of atomic columns and thus measures the low-frequency phonon modes, which to our knowledge is completely new. Combined with AIMD simulations, our results showed that Sb atoms have higher vibration amplitude than external Te atoms (as found in HAADF intensity profile study), and central Te atoms have the lowest amplitude, both in the directions perpendicular and parallel to the pseudo-vdW gaps. The perpendicular components are systematically higher than the parallel ones for all atom types. AIMD simulations showed that a 0.5 eV electronic excitation resulted in a minor increase in U values, with central Te atoms tending to have isotropic vibrations, probably due to perfect metavalence. Good agreements between our new methodology results and other experimental results (either X-ray and neutrons ones) or ab initio calculations tend to validate our methodology, but further works both experimental and numerical ones will be needed to confirm it completely. We hope that our results will stimulate other groups to test and use it. Overall, the quantitative HAADF analysis tools developed in the present work have been fully validated by their application to Sb_2Te_3 thin films for which a comparison with diffraction results can be made because the structure is periodic. The methods should be particularly important for GeTe/ Sb_2Te_3 SLs, comprising nonperiodic Sb_2Te_3 and GST blocks, for which diffraction studies alone may not provide a comprehensive understanding of the local atomic arrangement.

5. Experimental Section

Thin-Film Deposition: The Sb_2Te_3 films were deposited by high-vacuum magnetron sputtering. During the growth of Sb_2Te_3 films, the temperature was maintained at about 250 °C. Sputtering of a stoichiometric Sb_2Te_3 target leads to the deposition of Te-deficient films.[9,38] Therefore, following our previous studies,[9,37] the Sb_2Te_3 films were deposited by cosputtering Sb_2Te_3 target and an additional Te target. After deposition, all films were coated in situ with a 20 nm-thick layer of GeN to protect them from oxidation after fabrication.

TEM Thin-Foil Preparation: Lamellae for the TEM analysis were prepared by Ga^+ focused ion beam (FIB) milling using a ThermoFisher Scientific (TFS) Helios 450 machine. Prior to milling, two layers (first silicon oxide and then tungsten) were deposited to protect the top surface of the material. A 30 kV operation voltage for the initial milling was used and then the foil was thinned down to approximately 35 nm thick using a low beam energy in the range 5–8 kV to reduce FIB-induced damage.

ACOM Acquisition: The ACOM analysis was performed on a TFS Tecnai Osiris microscope operating at 200 kV and equipped with the NanoMEGAS ASTAR system. The microscope was set to a microprobe mode with a spot size of 10 using a 30 μm C_2 aperture. Diffraction patterns (consisted of 144 × 144 pixel images) were acquired on a Stingray charge coupled device camera with a 220 mm camera length (precisely calibrated using the diffraction patterns from the silicon substrate) using a 30 ms integration time. $1.4 \times 4.8\ \mu m^2$ mappings (cropped in Figure 1 for better visualization) with a step size of 10 nm were acquired for each sample. After indexing all the diffraction patterns, mappings were exported to ang file and subsequently imported (the format was modified using a separate Python file) in HKL Channel 5 software dedicated to process electron backscattered diffraction data. Angular disorientation maps of the Sb_2Te_3 grains with respect to the zone axis <11–20>condition were displayed using the ideal orientation manager.

STEM–HAADF Image Acquisition and Simulation: STEM–HAADF images were acquired on a probe-corrected TFS Titan Themis operated at 200 kV using a convergence semiangle of 18 mrad for the incident electron probe. The camera length of 86 mm corresponded to inner and outer collection angles of the HAADF detector (Fischione Model M3000) of 78 and 230 mrad. The shadow of the inner detector hole visible in the Ronchigram was not an accurate representation of the electron beam-sensitive region, which was measured according to the method of Lebeau et al.[57] Gun lens and spot size values were selected to provide a probe current of ≈20 pA. Settings of brightness/contrast were adjusted to ensure a linear contrast transfer of the amplifier. The normalization of experimental intensities to the incoming electron beam was performed using the detector scan, as explained in the Supporting Information S1. Series of 30 images were captured at a resolution of 2k × 2k, a pixel size of 3.13 pm, and a dwell time of 0.8 μs. Rigid registration for image alignment was performed using the SmartAlign software described in the study by Jones et al.[58] Simulations were carried out with the frozen lattice multislice method available in the STEMsim program[25] using five phonons for each simulation. We created the Sb_2Te_3 supercell using 6 × 2 unit cells along the <1120> direction. Maps were simulated with a pixel size of 5.28 pm for lamella thicknesses up to 105 nm with an increment corresponding to the slice thickness of 0.425 nm.

X-Ray Diffraction Experiment (XRD): XRD patterns were acquired in the in θ–2θ (Bragg Brentano) geometry using a D8 Bruker diffractometer equipped with a Ge monochromator selecting the Cu ($K\alpha_1$) radiation ($\lambda = 0.15406$ nm) and in-plane geometry, using a Rigaku SmartLab diffractometer (Cu $K\alpha_1$ and $K\alpha_2$ radiation).

Supporting Information

Supporting Information is available from the Wiley Online Library or from the author.

Acknowledgements

Part of this work was performed at the Platform for Nanocharacterization of the CEA Grenoble, MINATEC Campus, with support from the French Recherche Technologique de Base programme.

Conflict of Interest

The authors declare no conflict of interest.

Data Availability Statement

The data that support the findings of this study are available from the corresponding author upon reasonable request.

Keywords

chalcogenide phase-change materials, composition analyses, lattice parameters, Python libraries, Sb_2Te_3, scanning transmission electron microscopy–high-angle-annular dark-field images, thermal vibrations

Received: October 25, 2023
Revised: December 11, 2023
Published online:

 © 2024 Wiley-VCH GmbH

18626270, 0, Downloaded from https://onlinelibrary.wiley.com/doi/10.1002/pssr.202300402 by Thirion Paul - Dge, Wiley Online Library on [20/02/2024]. See the Terms and Conditions (https://onlinelibrary.wiley.com/terms-and-conditions) on Wiley Online Library for rules of use; OA articles are governed by the applicable Creative Commons License

[1] M. Longo, P. Fantini, P. Noé, *J. Phys. D: Appl. Phys.* **2020**, *53*, 440201.
[2] *Phase Change Memory* (Ed: A. Redaelli), Springer International Publishing, Cham **2018**.
[3] P. Noé, C. Vallée, F. Hippert, F. Fillot, J.-Y. Raty, *Semicond. Sci. Technol.* **2018**, *33*, 013002.
[4] R. E. Simpson, P. Fons, A. V. Kolobov, T. Fukaya, M. Krbal, T. Yagi, J. Tominaga, *Nat. Nanotechnol.* **2011**, *6*, 501.
[5] D. Térébénec, N. Castellani, N. Bernier, V. Sever, P. Kowalczyk, M. Bernard, M..-C. Cyrille, N.-P. Tran, F. Hippert, P. Noé, *Phys. Status Solidi RRL* **2021**, *15*, 2000538.
[6] J. Momand, R. Wang, J. E. Boschker, M. A. Verheijen, R. Calarco, B. J. Kooi, *Nanoscale* **2015**, *7*, 19136.
[7] J. Momand, F. R. L. Lange, R. Wang, J. E. Boschker, M. A. Verheijen, R. Calarco, M. Wuttig, B. J. Kooi, *J. Mater. Res.* **2016**, *31*, 3115.
[8] A. Lotnyk, I. Hilmi, U. Ross, B. Rauschenbach, *Nano Res.* **2018**, *11*, 1676.
[9] P. Kowalczyk, F. Hippert, N. Bernier, C. Mocuta, C. Sabbione, W. Batista-Pessoa, P. Noé, *Small* **2018**, *14*, 1704514.
[10] F. Acapito, P. Kowalczyk, J.-Y. Raty, C. Sabbione, F. Hippert, P. Noé, *J. Phys. D: Appl. Phys.* **2020**, *53*, 404002.
[11] A. Lotnyk, I. Hilmi, M. Behrens, B. Rauschenbach, *Appl. Surf. Sci.* **2021**, *536*, 147959.
[12] A. Lotnyk, U. Ross, T. Dankwort, I. Hilmi, L. Kienle, B. Rauschenbach, *Acta Mater.* **2017**, *141*, 92.
[13] A. Lotnyk, T. Dankwort, I. Hilmi, L. Kienle, B. Rauschenbach, *Nanoscale* **2019**, *11*, 10838.
[14] J.-J. Wang, J. Wang, Y. Xu, T. Xin, Z. Song, M. Pohlmann, M. Kaminski, L. Lu, H. Du, C.-L. Jia, R. Mazzarello, M. Wuttig, W. Zhang, *Phys. Status Solidi RRL* **2019**, *13*, 1900320.
[15] S. J. Pennycook, P. D. Nellist, *Scanning Transmission Electron Microscopy*, Springer, New York **2011**.
[16] B. Casarin, A. Caretta, J. Momand, B. J. Kooi, M. A. Verheijen, V. Bragaglia, R. Calarco, M. Chukalina, X. Yu, J. Robertson, F. R. L. Lange, M. Wuttig, A. Redaelli, E. Varesi, F. Parmigiani, M. Malvestuto, *Sci. Rep.* **2016**, *6*, 22353.
[17] A. B. Yankovich, B. Berkels, W. Dahmen, P. Binev, S. I. Sanchez, S. A. Bradley, A. Li, I. Szlufarska, P. M. Voyles, *Nat. Commun.* **2014**, *5*, 4155.
[18] T. Brieb, M. Tewes, M. Schowalter, K. Müller-Caspary, F. F. Frause, T. Mehrtens, J.-M. Hartmann, A. Rosenauer, *Ultramicroscopy* **2018**, *184*, 29.
[19] E. Abe, S. J. Pennycook, A. P. Tsai, *Nature* **2003**, *421*, 347.
[20] M. Nord, P. E. Vullum, I. MacLaren, T. Tybell, R. Holmestad, *Adv. Struct. Chem. Imaging.* **2017**, *3*, 9.
[21] K. Müller-Caspary, T. Mehrtens, M. Schowalter, T. Grieb, A. Rosenauer, F. F. Krause, C. Mahr, P. Potapov, in *European Microscopy Congress 2016, Proc.*, Lyon, France **2016**, pp. 481–482.
[22] A. De Backer, K. H. W. van den Bos, W. Van den Broek, J. Sijbers, S. Van Aert, *Ultramicroscopy* **2016**, *171*, 104.
[23] J.-M. Zuo, A. B. Shah, H. Kim, Y. Meng, W. Gao, J.-L. Rouvière, *Ultramicroscopy* **2014**, *136*, 50.
[24] A. Rosenauer, K. Gries, K. Müller, A. Pretorius, M. Schowalter, A. Avramescu, K. Engl, S. Lutgen, *Ultramicroscopy* **2009**, *109*, 1171.
[25] A. Rosenauer, M. Schowalter, *Microscopy of Semiconducting Materials* (Eds: A. G. Cullis, P. A. Midgley), Springer Proceedings in Physics, Vol. *120*, Springer, Dordrecht **2007**, pp. 170–172, https://doi.org/10.1007/978-1-4020-8615-1_36.
[26] A. Rosenauer, T. Mehrtens, K. Müller, K. Gries, M. Schowalter, P. V. Satyam, S. Bley, C. Tessarek, D. Hommel, K. Sebald, M. Seyfried, J. Gutowski, A. Avramescu, K. Engl, S. Lutgen, *Ultramicroscopy* **2011**, *111*, 1316.
[27] E. Longo, M. Belli, M. Alia, M. Rimoldi, R. Cecchini, M. Longo, C. Wiemer, L. Locatelli, P. Tsipas, A. Dimoulas, G. Gubbiotti, M. Fanciulli, R. Mantovan, *Adv. Funct. Mater.* **2022**, *32*, 210936.
[28] S. Teresi, N. Sebe, J. Patterson, T. Frottier, A. Kandazoglou, P. Noël, P. Sgarro, D. Térébénec, N. Bernier, F. Hippert, J.-P. Attané, L. Vila, P. Noé, M. Cosset-Chéneau, *Adv. Funct. Mater.* **2023**, *32*, 2303878.
[29] R. Venkatasubramanian, E. Siivola, T. Colpitts, B. O'Quinn, *Nature* **2001**, *413*, 597.
[30] M. Tan, Y. Deng, Y. Wang, B. Luo, L. Liang, L. Cao, *J. Electron. Mater.* **2012**, *41*, 3031.
[31] Y. Saito, P. Fons, A. V. Kolobov, J. Tominaga, *Phys. Status Solidi B* **2015**, *252*, 2151.
[32] Y. Saito, P. Fons, L. Bolotov, N. Miyata, A. V. Kolobov, J. Tominaga, *AIP Adv.* **2016**, *6*, 045220.
[33] M. Lanius, J. Kampmeier, S. Kölling, G. Mussler, P. M. Koenraad, D. Grützmacher, *J. Cryst. Growth* **2016**, *453*, 158.
[34] I. Hilmi, A. Lotnyk, J. W. Gerlach, P. Schumacher, B. Rauschenbach, *APL Mater.* **2017**, *5*, 050701.
[35] J. E. Boschker, E. Tisbi, E. Placidi, J. Momand, A. Redaelli, B. J. Kooi, F. Arciprete, R. Calarco, *AIP Adv.* **2017**, *7*, 015106.
[36] J. Momand, J. E. Boschker, R. Wang, R. Calarco, B. J. Kooi, *CrystEngComm* **2018**, *20*, 340.
[37] F. Hippert, P. Kowalczyk, N. Bernier, C. Sabbione, X. Zucchi, D. Térébénec, C. Mocuta, P. Noé, *J. Phys. D: Appl. Phys.* **2020**, *53*, 154003.
[38] Y. Saito, P. Fons, A. V. Kolobov, K. V. Mitrofanov, K. Makino, J. Tominaga, S. Hatayama, Y. Sutou, M. Hase, J. Robertson, *J. Phys. D: Appl. Phys.* **2020**, *53*, 284002.
[39] T. L. Anderson, H. B. Krause, *Acta Cryst. B* **1974**, *30*, 1307.
[40] K. A. Kokh, V. V. Atuchin, T. A. Gavrilova, N. V. Kuratieva, N. V. Pervukhina, N. V. Surovtsev, *Solid State Commun.* **2014**, *177*, 16.
[41] A. N. Mansour, W. Wong-Ng, Q. Huang, W. Tang, A. Thompson, J. Sharp, *J. App. Phys.* **2014**, *116*, 083513.
[42] E. F. Rauch, J. Portillo, S. Nicolopoulos, D. Bultreys, S. Rouvimov, P. Moeck, *Z. Kristal.* **2010**, *225*, 103.
[43] D. L. Medlin, Q. M. Ramasse, C. D. Spataru, N. Y. C. Yang, *J. App. Phys.* **2010**, *108*, 043517.
[44] Y. Cheng, O. Cojocaru-Mirédin, J. Keutgen, Y. Yu, M. Küpers, M. Schumacher, P. Golub, J.-Y. Raty, R. Dronskowski, M. Wuttig, *Adv. Mater.* **2019**, *31*, 1904316.
[45] L. E. Shelimova, O. G. Karpinskii, M. A. Kretova, V. I. Kosyakov, V. A. Shestakov, V. S. Zemskov, F. A. Kuznetsov, *Inorg. Mater.* **2000**, *36*, 768.
[46] A. Lotnyk, T. Dankwort, I. Hilmi, L. Kienle, B. Rauschenbach, *Scr. Mater.* **2019**, *166*, 154.
[47] J. M. LeBeau, S. D. Findlay, L. J. Allen, S. Stemmer, *Ultramicroscopy* **2010**, *110*, 118.
[48] A. Rosenauer, M. Schowalter, J. T. Titantah, D. Lamoen, *Ultramicroscopy* **2008**, *108*, 1504.
[49] K. N. Trueblood, H.-B. Bürgi, H. Burzlaff, J. D. Dunitz, C. M. Gramaccioli, H. H. Schulz, U. Shmueli, S. C. Abrahams, *Acta Cryst.* **1996**, *A52*, 770.
[50] K. Aso, K. Shigematsu, T. Yamamoto, S. Matsumura, *Microscopy* **2016**, *65*, 391.
[51] Z. Chen, Y. Jiang, Y. T. Shao, M. E. Holtz, M. Odstrcil, M. Guizar-Sicairos, I. Hanke, S. Ganschow, D. G. Schlom, D. A. Muller, *Science* **2021**, *372*, 826.
[52] W. Wang, W. Cai, *RSC Adv.* **2021**, *11*, 11057.
[53] G. Kresse, D. Joubert, *Phys. Rev. B* **1999**, *59*, 1758.
[54] P. E. Blöchl, *Phys. Rev. B* **1994**, *50*, 17953.
[55] J. P. Perdew, A. Ruzsinszky, G. I. Csonka, O. A. Vydrov, G. E. Scuseria, L. A. Constantin, X. Zhou, K. Burke, *Phys. Rev. Lett.* **2008**, *100*, 136406.
[56] W. Ibarra-Hernández, J.-Y. Raty, *Phys. Rev. B* **2018**, *97*, 245205.
[57] J. M. Lebeau, S. Stemmer, *Ultramicroscopy* **2008**, *108*, 1653.
[58] L. Jones, H. Yang, T. J. Pennycook, M. S. J. Marshall, S. Van Aert, N. D. Browning, M. R. Castell, P. D. Nellist, *Adv. Struct. Chem. Imaging* **2015**, *1*, 8.

© 2024 Wiley-VCH GmbH

18626270, 0, Downloaded from https://onlinelibrary.wiley.com/doi/10.1002/pssr.202300402 by Thirion Paul - Dge, Wiley Online Library on [20/02/2024]. See the Terms and Conditions (https://onlinelibrary.wiley.com/terms-and-conditions) on Wiley Online Library for rules of use; OA articles are governed by the applicable Creative Commons License